# A 2.2 nW Analog Electrocardiogram Processor based on Stochastic Resonance Achieving a 99.94% QRS Complex Detection Sensitivity

Cihan Berk Güngör, *Graduate Student Member, IEEE*, Patrick P. Mercier, *Senior Member, IEEE*, and Hakan Töreyin, *Member, IEEE* 

Abstract—This paper presents an ultra-low power electrocardiogram (ECG) processor that can detect QRSwaves in real time as the data streams in. The processor performs out-of-band noise suppression via a linear filter, and in-band noise suppression via a nonlinear filter. The nonlinear filter also enhances the QRS-waves by facilitating stochastic resonance. The processor identifies the QRSwaves on noise-suppressed and enhanced recordings using a constant threshold detector. For energy-efficiency and compactness, the processor exploits current-mode analog signal processing techniques, which significantly reduces the design complexity when implementing the second-order dynamics of the nonlinear filter. The processor is designed and implemented in TSMC 65 nm CMOS technology. In terms of detection performance, the processor achieves an average F1 = 99.88% over the MIT-BIH Arrhythmia database and outperforms all previous ultra-low power ECG processors. The processor is the first that is validated against noisy ECG recordings of MIT-BIH NST and TELE databases, where it achieves better detection performances than most digital algorithms run on digital platforms. The design has a footprint of 0.08 mm<sup>2</sup> and dissipates 2.2 nW when supplied by a single 1V supply, making it the first ultra-low power and real-time processor that facilitates stochastic resonance.

Index Terms—Energy-efficient IC processor, physical computation, stochastic resonance, QRS-wave, real-time signal processing.

#### I. INTRODUCTION

LECTROCARDIOGRAM (ECG) is an electrical biopotential

The paper was submitted on October 20, 2022 for review. This material is based upon work supported by the National Science Foundation under Grant Number 1916160.

C. B. Güngör is with the Department of Electrical and Computer Engineering, University of California at San Diego, La Jolla, CA 92093 USA and with the Department of Electrical and Computer Engineering, San Diego State University, San Diego, CA 92182 USA (e-mail: cgungor@ucsd.edu).

P. P. Mercier is with the Department of Electrical and Computer Engineering, University of California at San Diego, La Jolla, CA 92093 USA (e-mail: pmercier@ucsd.edu).

H. Töreyin is with the Electrical and Computer Engineering Department, San Diego State University, San Diego, CA 92182 USA, (e-mail: htoreyin@sdsu.edu).

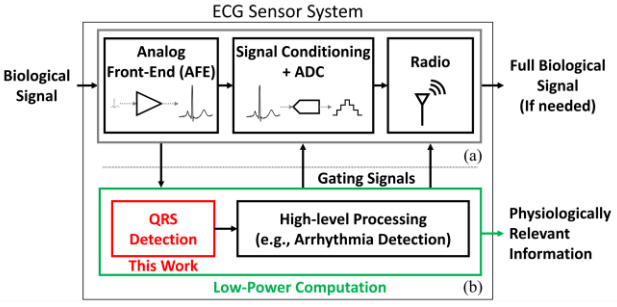


Fig. 1. ECG sensor system block diagram. (a) A conventional system. (b) On-site, real-time and low power ECG processing can allow gating of power-hungry blocks, thereby reducing the total system power.

originated from the heart muscle, and it represents important cardiac and autonomic regulation information. Therefore, ECG has been a major biosignal for assessment of cardiovascular and autonomic nervous system [2] health.

Advances in body sensor technologies have allowed ECG monitoring for extended periods, thereby enabling detection of rare cardiac cycle abnormalities [3], [4]. Among different ECG sensor systems, injectables [5] and implantables [6] are more comfortable than wearables for long term use [7]. The convenience, however, is achieved by having compact form factors, which limits the battery capacity. Therefore, to minimize charging frequency in daily use or frequent replacements of low-capacity batteries in the long term, strict power consumption constraints are imposed on these systems.

Conventional injectable/implantable ECG sensors operate on batteries with capacities ranging from a few  $\mu$ Ah to a few tens of mAh [8], [9]. Typically, the battery powers three major blocks; namely analog front-end (AFE), signal conditioning and analog-to-digital converter (ADC), and radio (Fig. 1(a)). Of these, radio typically dissipates orders of magnitude greater power than the other blocks. For instance, the lowest reported power of those blocks in the literature is 20  $\mu$ W [10] for the radio, in contrast to 1.05 nW [6] and 1.1 nW [6] for the AFE and ADC, respectively. Therefore, improvements in radio power consumption would also significantly improve the system power dissipation.

One possible approach to reduce the radio power is

minimizing the volume of data that must be transmitted. Alternative sampling techniques such as adaptive sampling [11], compressed sensing [12], and entropy encoder [13] shrink the data volume. Although these approaches achieve more than 60% data compression [13], and thus reduce both ADC and radio power dissipation; there is more room for improvement in long term ECG monitoring applications: Specifically, in arrhythmia detection and autonomic regulation assessment, which are among the most common use cases of implantable and injectable ECG monitoring systems, the most important feature to detect and analyze is the QRS-wave [2], [7], [14]. The QRS-wave duration can range between 80 ms and 120 ms [15]. Therefore, considering a heart rate range of 30 beats per minute (bpm) and 240 bpm [16], [17], by activating the ADC and radio to transmit only the QRS waves would reduce the data volume by at least 52% and as much as 96%. It is noteworthy that, the aforementioned alternative sampling techniques can be applied on only the QRS-waves to achieve additional data volume compression.

Notably, in addition to potentially achieving significant data compression and consequent power consumption reduction, on-chip QRS-wave detection is particularly appropriate from time sensitivity and privacy perspectives of ECG monitoring. By detecting the heart beats and identifying the rare arrhythmia events on site at the ECG node also minimizes the dependence to the radio link (Fig. 1(b)), which could suffer from poor data connections leading to delays in transmission of time sensitive information [10] or channel attacks targeting the sensitive health data [18].

Transmission of only the QRS-waves necessitates on-chip QRS-wave detection [13], [15]. Furthermore, since the detection should be continuously performed, to fully benefit from the power savings of data compression, the additional power consumption of a QRS-wave detection processor should be significantly smaller than that of the radio and comparable to that of the AFE, which is the other block that is constantly on. This study focuses on design and validation of such an energy-efficient QRS-wave detection processor (Fig. 1(b)).

Several on-chip ECG processors identify the QRS-waves with high accuracy, while remaining below the strict power consumption target of a few nW [5], [15], [19]–[21]. In all these systems, first, a pre-processing stage enhances the QRS-waves while suppressing noise. Pre-processing is followed by detection, which is typically performed by thresholding the enhanced QRS-waves. Therefore, in this scheme, detection accuracy strongly depends on the pre-processing stage performance. In fact, the processors implementing more complicated noise suppression and QRS-wave enhancement techniques (e.g., curve length transform [15] or wavelet transform [22]) also report better detection performance than those implementing simpler enhancement methods (e.g., amplitude thresholding [19] or band-pass filtering [23]).

On the flip side, to a first order approximation, algorithm complexity increases power consumption. A remedy for power consumption is leveraging analog signal processing (ASP) instead of digital signal processing (DSP) techniques to implement an algorithm. To illustrate, a digital implementation

of the popular Pan-Tompkins (PT) algorithm consumes 2.78  $\mu W$  [24], three orders of magnitude more power than an ASP implementation in the same technology based on the PT algorithm in [25]. While transforming an algorithm originally designed in the digital domain into the analog domain is attractive for power savings, a one-to-one mapping across the domains is not always possible. For instance, the adaptive thresholding obtained as a weighted sum of the QRS-wave peaks and the noise level of the full recording in the original PT algorithm [26] is replaced with hard-thresholding in the ASP version [25] for a memory-free fully analog implementation. With this simplification in the design, detection sensitivity is compromised (i.e., 99.83% in a digital PT [24] vs. 99.63% [25]).

In this study, the overarching goal is to significantly enhance the battery life of implantable and injectable ECG monitoring systems. To achieve the goal, the study aims to significantly reduce the data volume, and thus potentially minimize the radio power, by detecting the important features of ECG, namely QRS-waves, in real-time and in an ultra-low power manner. In doing so, this work follows a different QRS-wave enhancement approach that has direct physical computing roots, and thus enabling a natural and efficient implementation as an ASP algorithm in silicon. The QRS-wave enhancement engine of the ECG processor is a nonlinear filter. Notably, the filter facilitates stochastic resonance (SR), where the noise existing in the signal assists the filter in enhancing the QRS-waves. Accordingly, the study shows that, even in noisy recordings, the nonlinear filter leads to high QRS-wave detection performance.

A numerical analysis of the nonlinear filter performing QRSwave detection was presented in [27]. Furthermore, a circuit implementation of the filter was introduced with only schematic-level simulation results in [28]. Unlike those previous studies, this work, for the first time, experimentally demonstrates an ultra-low power implementation of an ECG processor system that has the proposed nonlinear filter at its core. The processor detects the ORS-waves truly in real-time as digitally amplified ECG recordings from multiple ECG databases are streamed in. The study presents measurement results characterizing the different blocks of the processor and the QRS-wave detection performance of the full system in detail. The novelties of the work are (1) presenting the experimental results of a nonlinear filter that enhances QRSwaves in an ECG by facilitating stochastic resonance, (2) demonstrating an ultra-low power and real-time processor that facilitates stochastic resonance, and (3) validating an ultra-low power and real-time ECG processor against noisy MIT-BIH NST and TELE databases.

In Section II, the nonlinear filter and its mechanisms for noise suppression and QRS-wave enhancement are presented. In Section III, the circuit implementation of the ECG processor is discussed. In Section IV, measurement results of QRS-wave detection in three major benchmarking databases are presented, which is followed by the discussion of the results in Section V. The paper is concluded in Section VI.

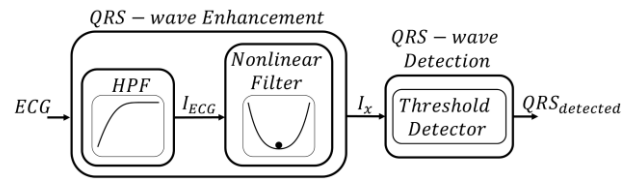


Fig. 2. Block diagram of the proposed QRS-wave detector.

#### II. NONLINEAR FILTERING FOR QRS-WAVE ENHANCEMENT

The block diagram of the proposed ECG processor is shown in Fig. 2. QRS-wave enhancement is achieved through two filters, a high-pass filter (HPF) and a novel nonlinear filter. The HPF is a 1<sup>st</sup> order linear filter with cut-off frequency set at 1 Hz to suppress the low-frequency baseline wander. Properties of the novel nonlinear filter and its mechanisms for in-band noise suppression and QRS-wave enhancement are presented in the rest of this section.

#### A. Nonlinear Filter Overview

To take advantage of the noise existing in an ECG signal when enhancing the ORS-waves, the nonlinear filter implements the dynamics of a particle inside a well potential, which is a system widely used in the literature studying signal enhancement by facilitating noise, namely stochastic resonance (SR) [29]. Following numerical analyses on different potential shapes and damping scenarios [30], high SNR improvements for QRS-waves are demonstrated when the system is an underdamped monostable potential well in [27] (Fig. 3). In this system, the particle moves inside the well potential under the influence of two forces,  $f_{ECG}(t)$  and  $f_{well}(x,t)$ . Of these forces exerted onto the particle, the former is the input of the system, ECG, and the latter is the force applied by the monostable well potential,  $U(x,t) = \alpha x(t)^2/2$ , towards the stable point with  $f_{well}(x,t) = -dU(x,t)/dx = -ax(t)$ , where a determines the steepness of the well. The output of the system is the projection of the particle on the x-axis, x(t). The differential equation governing the dynamics of this system is presented in Section III.B.

#### B. In-Band Noise Suppression

The nonlinear filter performs in-band noise suppression on accounts of the presence of a stable point in the system. Accordingly, when  $f_{ECG}$  is small; such as ECG portions outside the prominent QRS-wave, P-wave, or T-wave features;  $f_{well}$  rapidly balances  $f_{ECG}$  out. Therefore,  $f_{ECG}$  cannot move the particle considerably away from the stable point, which causes the particle to swing within a proximity around the stable point and keeps the output, x(t), small.

#### C. QRS-Wave Enhancement

Two mechanisms are responsible from QRS-wave enhancement: (i) large  $f_{ECG}$  during the QRS-waves and (ii) SR. Large  $f_{ECG}$  during QRS-waves can move the particle outside the stable point, and thus increasing the x(t) amplitude. Additionally, the system exhibits SR, where a noisy  $f_{ECG}$  can help the particle reach greater x(t) compared to a noise-free  $f_{ECG}$ . In this system, it is essential to have an optimum noise intensity that is large enough to observe the aid of noise and small enough to prevent ECG from being swamped by noise.

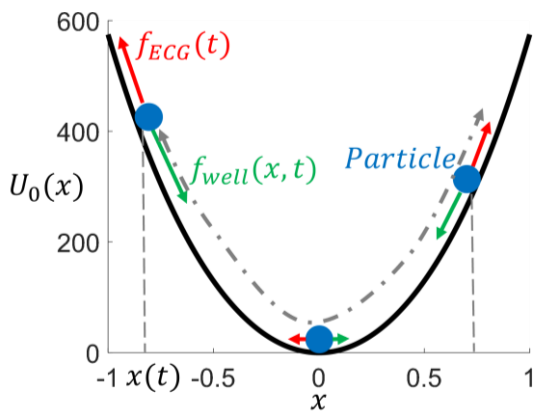


Fig. 3. A nonlinear system facilitating stochastic resonance is a particle in an underdamped monostable well. The forces,  $f_{ECG}(t)$  and  $f_{well}(x,t)$ , acting on the particle are shown for different particle locations.

Facilitation of SR in a system of particle inside a monostable well is theoretically verified in [31]. Verification of SR on the physical implementation of the system is presented in Section IV.C.

#### III. ECG PROCESSOR

The ECG processor is designed in TSMC 65nm CMOS technology. To minimize gate leakage, high-voltage devices are used. Two major points are considered when transforming the digital algorithm in [27] into the analog domain.

The first consideration is achieving design simplicity to minimize power, area, and noise. Analog processing offers better power and area efficiency than digital for smaller effective resolution levels (i.e., six to eight bits of effective resolution). However, one should be particularly careful with the noise in the circuit, which increases with design complexity, since unlike digital processing, analog computing does not offer bit correction. To reduce complexity, this work follows three design choices: (i) Unlike digital processors, where voltage is used to represent digitized levels of information, in analog, the designer has the liberty to represent the continuous information as current or voltage. To easily interface with a preceding analog front-end stage feeding the ECG signals and control a succeeding signal conditioning and radio blocks following the QRS-wave detection, the processor is designed to receive voltage inputs and generate voltage pulses. On the other hand, to efficiently perform the several signal manipulations in the processing chain (e.g., multiplications, additions/subtractions, differentiation, etc.), the information is presented as current signals inside the processing chain. (ii) While transforming the developed digital nonlinear filter into the analog domain, the processor uses a simplified version of the monostable well potential function used in the simulation-based nonlinear filtering studies presented in [27] and [28], which form the bases of this work. The monostable well in Fig. 3 is represented by a  $2^{nd}$  order function,  $\alpha x^2/2$ , rather than a  $4^{th}$  order function,  $ax^2/2 + bx^4/4$ , informed by a previous study showing the insignificance of the 4th order term on the nonlinear filter dynamics [32]. (iii) A 1st order high-pass filter is implemented instead of a higher-order band-pass filter in the digital version of the algorithm in [27] and [28]. The high-pass filter is preferred as the baseline wander is more problematic than high

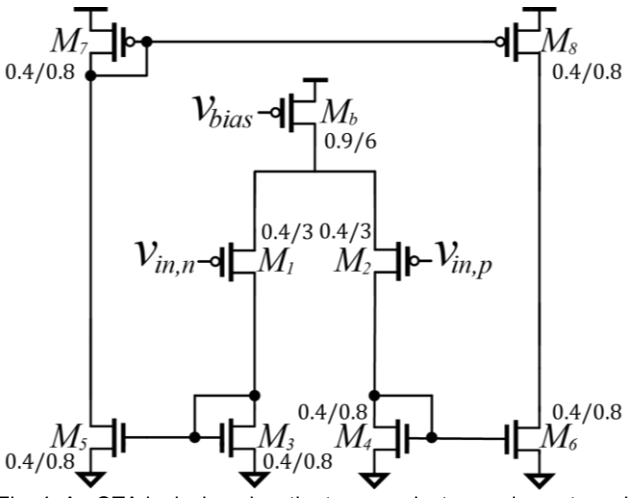


Fig. 4. An OTA is designed as the transconductance element used in the processor. Device sizes are given as *width/length* in µm.

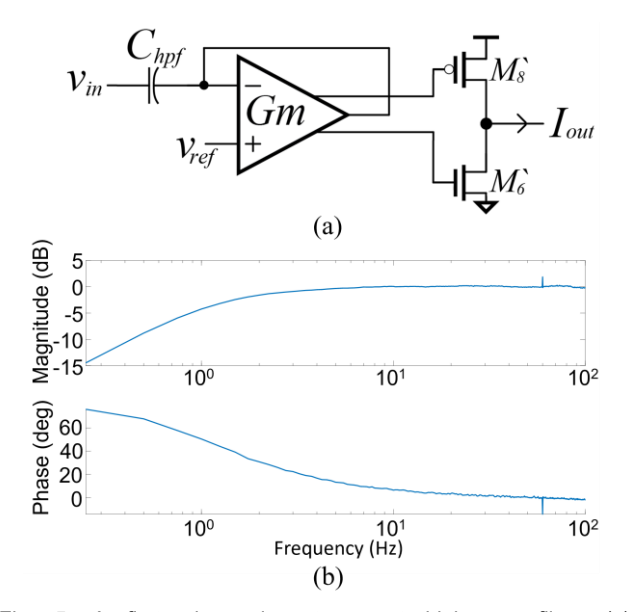


Fig. 5. A first-order voltage-to-current high-pass filter. (a) Schematic. (b) Frequency response.

frequency noise for nonlinear filter circuitry. The designed high-pass filter also converts the voltage input into current for the rest of the processor.

The second consideration is related to the difference between solving a differential equation in analog and digital. In digital, solution of the generalized Langevin equation, which is a 2<sup>nd</sup> order differential equation, is approximated using numerical solvers such as the Runge-Kutta method. On the other hand, solving a differential equation in analog translates into implementing the differential equation in silicon using circuit elements, which in real-time solves for the desired variable without approximations. In implementing the differential equation in analog circuit shown in Fig. 6, it is ensured that the integration is achieved within the ECG bandwidth.

The design is supplied by an external power supply of 1 V and all bias voltages are provided externally. Throughout the design, identical operational transconductance amplifiers (OTAs) are used. For energy-efficiency and compactness, all devices of the pMOS-input OTA are sized to operate in weak inversion saturation with the device sizes presented in Fig. 4.

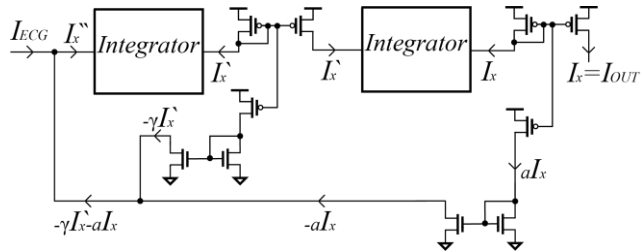


Fig. 6. The closed-loop block diagram of the proposed nonlinear filter implementing the dynamics of the monostable well in Fig. 3.

The output current-input voltage relationship demonstrates a transconductance of 85 pS with an input linear range of 90 mV. The maximum gain is measured as 28 dB and the unity-gain bandwidth is measured as 2.7 kHz. When biased with 10 pA (the bias current of the integrators), the OTA dissipates 30 pW and the area consumption of a single OTA is 0.00484 mm². Compared with recent OTAs used in analog signal processing applications [33]–[35], the designed OTA achieves a high gain-bandwidth product (GBW) per power and area. Specifically, the OTA demonstrates a GBW per nW\*mm² of 20.25 MHz as opposed to <50 kHz of the designs in [33] and [34].

The blocks of the ECG processor are detailed below.

### A. High-Pass Filter

The band-pass filter (HPF) is designed as a 1<sup>st</sup>-order voltage-to-current transconductance stage (Fig. 5(a)). The OTA output current is copied using M8' and M6' devices in Fig. 5(a), which serve as additional outputs for the M7-M8 and M4-M6 mirrors in Fig. 4. The filter has the transfer function:

$$\frac{I_{out}(s)}{V_{in}(s)} = -\frac{sC_{hpf}}{1 + sC_{hnf}/G_m} \tag{1}$$

where  $C_{hpf} = 10 \ pF$ . The OTA is biased with 10 pA to achieve a transconductance of 10 pS and cut-off frequency at 1 Hz, as shown in Fig. 5(b).

#### B. Nonlinear Filter

The dynamics of the nonlinear system shown in Fig. 3 are governed by the generalized Langevin equation [27], [28]:

$$\frac{d^2I_x(t)}{dt^2} + \gamma \frac{dI_x(t)}{dt} = -aI_x + I_{ECG}(t),\tag{2}$$

where the left-hand side governs force terms proportional to the acceleration and velocity of the particle and the right-hand side terms are respectively the  $f_{well}$  and  $f_{ECG}$  in Fig. 3. In (2),  $\gamma$  is damping constant, a is monostable well potential constant, and  $I_{ECG}(t)$  is high-pass filtered ECG signal. The output of (2) is implemented as a current variable,  $I_x$ , which is obtained through a closed-loop system presented in Fig. 6. The integrator outputs are scaled to reflect the values of the damping constant,  $\gamma = 20$ , and well potential constant,  $\alpha = 1$ ; and fed back to the input node. Integrator output scaling is performed via cascode current mirrors.

The selection of a and  $\gamma$  are informed by their effects on SNR improvement [27], [30], which is evaluated numerically in MATLAB (MathWorks, Natick, MA, USA) using the

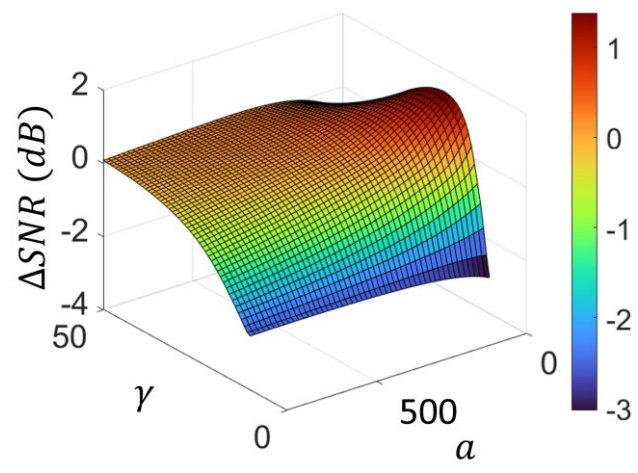


Fig. 7. The SNR improvement of the nonlinear filter with respect to a and  $\gamma$ . The results are obtained using the recording 100 of the MIT-BIH Arrhythmia database.

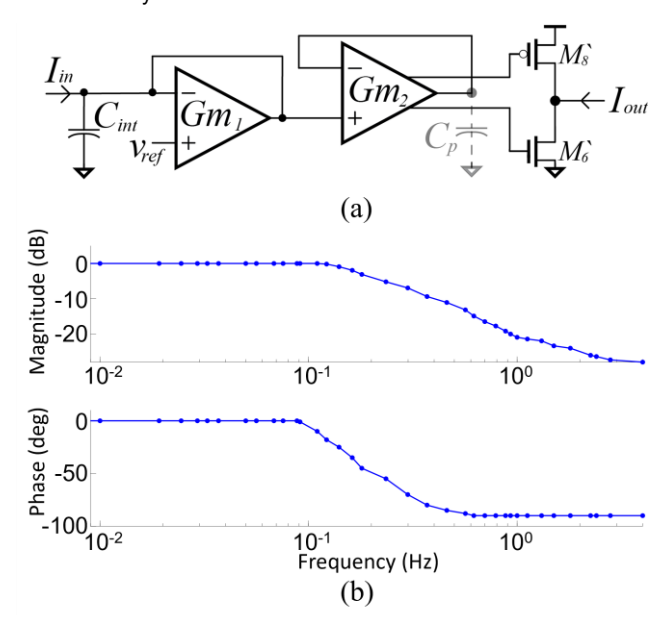


Fig. 8. Current-to-current integrator. (a) Schematic. Both OTAs have the same schematic given in Fig. 4. (b) Frequency response.

recording 100 of the MIT-BIH Arrhythmia database [36]. Here, signal-to-noise ratio (SNR) is defined as:

$$SNR = 20log\left(\frac{A_{pp} \ of \ QRS-waves}{Standard \ deviation \ of \ a \ noise \ segment}\right), \quad (3)$$

where  $A_{pp}$  is the average peak-to-peak amplitude of 100 arbitrarily selected QRS-waves. QRS regions are segmented as 100 ms time windows centered around the true QRS-wave points. The 100 QRS-wave point set consists of one automatically and arbitrarily selected QRS-wave point using the rand function of MATLAB and the 99 QRS-wave points succeeding it. For noise standard deviation, 100 noise segments (~1 s each) are selected arbitrarily inside the sections between the selected QRS-wave segments. It is noteworthy that, with the target of this study being QRS-wave detection, all ECG signal portions outside the QRS-wave segments are counted as noise. The SNR improvement ( $\Delta SNR$ ) is calculated as  $\Delta SNR = SNR_{out} - SNR_{in}$  where  $SNR_{in}$  and  $SNR_{out}$  are input and

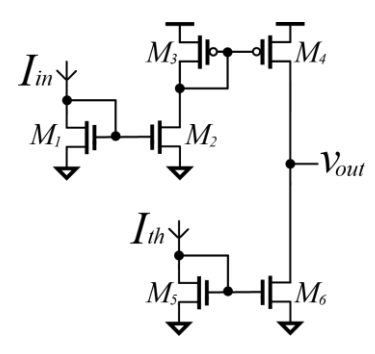


Fig. 9. Current comparator.

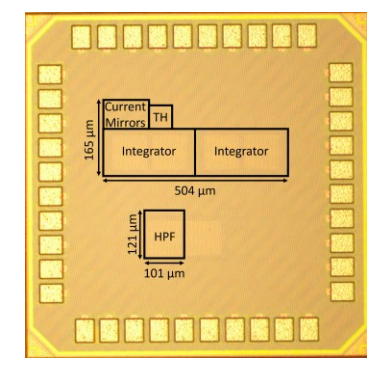


Fig. 10. Die photo.

output SNRs calculated with (3).  $\Delta SNR$  peaks at a=1 and  $\gamma=20$  as shown in a parametric sweep in Fig. 7.

To facilitate current-mode signal processing, the integrators are designed as current-input and current-output (Fig. 8). An integrator consists of two OTAs, where the 1<sup>st</sup> and the 2<sup>nd</sup> OTAs respectively serve as a transimpedance integrator stage and a transconductance stage. Both OTAs have the same schematic as given in Fig. 4. By mirroring the devices at the output branch of the 2<sup>nd</sup> OTA, the integrator output is equal to the output current of the 2<sup>nd</sup> OTA. With a parasitic capacitance,  $C_p$ , at the output node of the 2<sup>nd</sup> OTA, the transfer function consists of two poles at  $p_1 = C_{int}/Gm_1$  and  $p_2 = C_p/Gm_2$ , and a zero at 0 Hz:

$$\frac{I_{out}(s)}{I_{in}(s)} = \frac{sC_p/Gm_1}{(1+sp_1)(1+sp_2)} \tag{4}$$

In (4), the gain is controlled by  $C_p/Gm_1$ . For integration over the ECG bandwidth of [0.5-100] Hz, the poles are placed at 0.1 Hz and 500 Hz by setting  $Gm_1$  and  $Gm_2$  values as 10 pS and 65 nS (Fig. 8(b)).

#### C. Threshold Detector

The threshold detector is implemented as a current comparator that compares the nonlinear filter output  $I_x$  with a dc threshold,  $I_{th}$  (Fig. 9). When  $I_{th}$  is higher (lower) than  $I_{in}$ , the output voltage,  $V_{out}$ , is pulled to a low (high) voltage by  $M_6$  ( $M_4$ ). For a recording,  $I_{th}$  is kept constant. However, for each recording,  $I_{th}$  is individually set in multiples of 0.1 nA to maximize QRS-wave detection performance quantified using the F1 score explained in Section IV.D. The  $I_{th}$  value is set at 0.1 nA for most of the ECG recordings across databases.



Fig. 11. Measurement setup. The acquisition PC is used to control the Digilent Analog Discovery 2 devices, which supply the bias voltages and feed the ECG recording to the processor. B2901BL and B2912A sourcemeters are used to characterize the integrators and the nonlinear filter, where the B2912A sources input currents and B901BL measures output currents of the block under test.

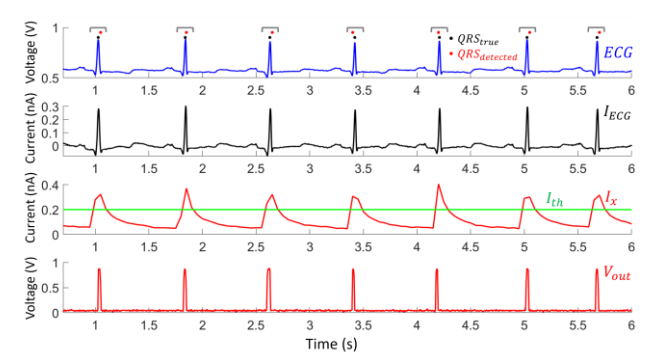


Fig. 12. Waveforms from the processing chain for a 6 s portion of a recording. SNR improvement for this portion is  $\Delta SNR = 0.42~dB$ . From top to bottom; the raw ECG signal; the high-pass filtered ECG current signal,  $I_{ECG}$ ; the nonlinear filter output,  $I_x$ ; and the threshold detector output  $V_{out}$  are shown. The true and detected QRS-wave positions are shown on the top row with black and red dots, respectively. The third raw also shows the threshold  $I_{th}$  level. The gray brackets on the top row indicate the search windows used to evaluate the QRS-wave detection performance as explained in Section IV.D.

#### IV. RESULTS

The total area of the processor is 0.08 mm<sup>2</sup> (Fig. 10). The processor dissipates 2.2 nW when supplied by a single 1 V. Area and power dissipation breakdown are as follows: Highpass filter consumes 0.1 nW and 0.012 mm<sup>2</sup>, integrators consume 1.9 nW and 0.061 mm<sup>2</sup>, current mirrors consume 0.15 nW and 0.005 mm<sup>2</sup>, and threshold detector consumes 0.05 nW and 0.002 mm<sup>2</sup>.

#### A. Measurement Setup

The measurement setup is shown in Fig. 11. A printed circuit board (PCB) interface is designed to interface the chip with the measurement instruments. Analog Discovery 2 (Digilent, Pullman, WA) instruments are used for supplying the 1 V and bias voltages, as well as supplying the analog ECG recordings to the processor after performing 14-bit digital-to-analog conversion of the recordings at frequencies that match the original sampling rates (i.e., 360 Hz for MIT-BIH Arrhythmia and MIT-BIH NST databases, and 500 Hz for TELE database). B2912A and B2901BL sourcemeters (Keysight Technologies, Santa Rosa, CA), an SRS SR785 spectrum analyzer (Stanford Research Systems, Sunnyvale, CA), and an MSOX3024T oscilloscope (Keysight Technologies, Santa Rosa, CA) are used to individually characterize the blocks. For precise current measurements, the chip is connected to the sourcemeters via

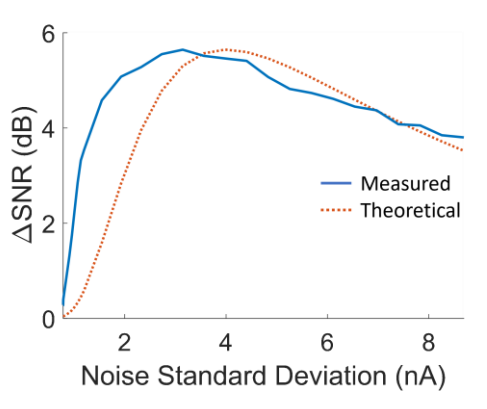


Fig. 13. A 6 s portion of the recording 100 of the MIT-BIH Arrhythmia database is added with increasing intensities of noise and the SNR improvement is measured. The SNR improvement displays the characteristic bell curve shape of SR and peaks at a noise standard deviation of 3.15 nA. The theoretical expectation of SNR improvement with noise obtained using the Fokker-Planck equation displays a similar trend.

N1294A-001 banana-triax adapters. The voltage waveform outputs of the processor are captured using an MP 160 data acquisition system (Biopac Systems Inc., Goleta, CA), for detection performance assessment on MATLAB. For illustration purposes, nonlinear filter current output waveforms,  $I_x$ , are captured by the B2912A sourcemeter.

Waveforms from the processing chain corresponding to an exemplary six second portion of the recording 100 from the MIT-BIH Arrhythmia database [36] are presented in Fig. 12.

#### B. In-Band Noise Suppression Assessment

To verify the in-band noise suppression of the nonlinear filter, three ECG recordings from the MIT-BIH Arrhythmia databases are used [36]. First, QRS-wave segments in ECG signal and nonlinear filter output are identified by selecting 100 ms time windows around the true QRS-waves. Then, the ECG portions between the selected QRS-wave segments are identified as noise sections. Notably, although such ECG portions include other physiologically important ECG features (e.g., P-wave and T-wave), they are undesired from QRS-wave detection perspective. Among all noise sections, ECG in-band ([0.5-100 Hz]) power of arbitrarily-selected 100 of them are calculated both for the input,  $I_{ECG}$  and the output,  $I_x$  signals. The average power decrease for the recordings are calculated as 8.83 dB, 8.6 dB, and 8.58 dB respectively for low- (#103), medium- (#116), and high-noise (#207) recordings.

#### C. Demonstration of Stochastic Resonance in QRS-Wave Enhancement

The SR facilitation in the nonlinear filter is demonstrated using an exemplary 6 s portion of one of the cleanest recordings (#100) of the MIT-BIH Arrhythmia database. White Gaussian noise at varying standard deviations,  $\sigma$ , were added digitally on the recording in MATLAB and fed to the nonlinear filter. The nonlinear filter outputs are stored and  $\Delta SNR$  is calculated as described in (3), this time using only eight QRS-waves. The SNR improvement obtained by the nonlinear filter in Fig. 13 demonstrates the characteristic bell curve of SR, where an optimum additive non-zero white Gaussian noise intensity ( $\sigma = 3.15 \ nA$ ) maximizes  $\Delta SNR$ . Notably, this behavior is in line

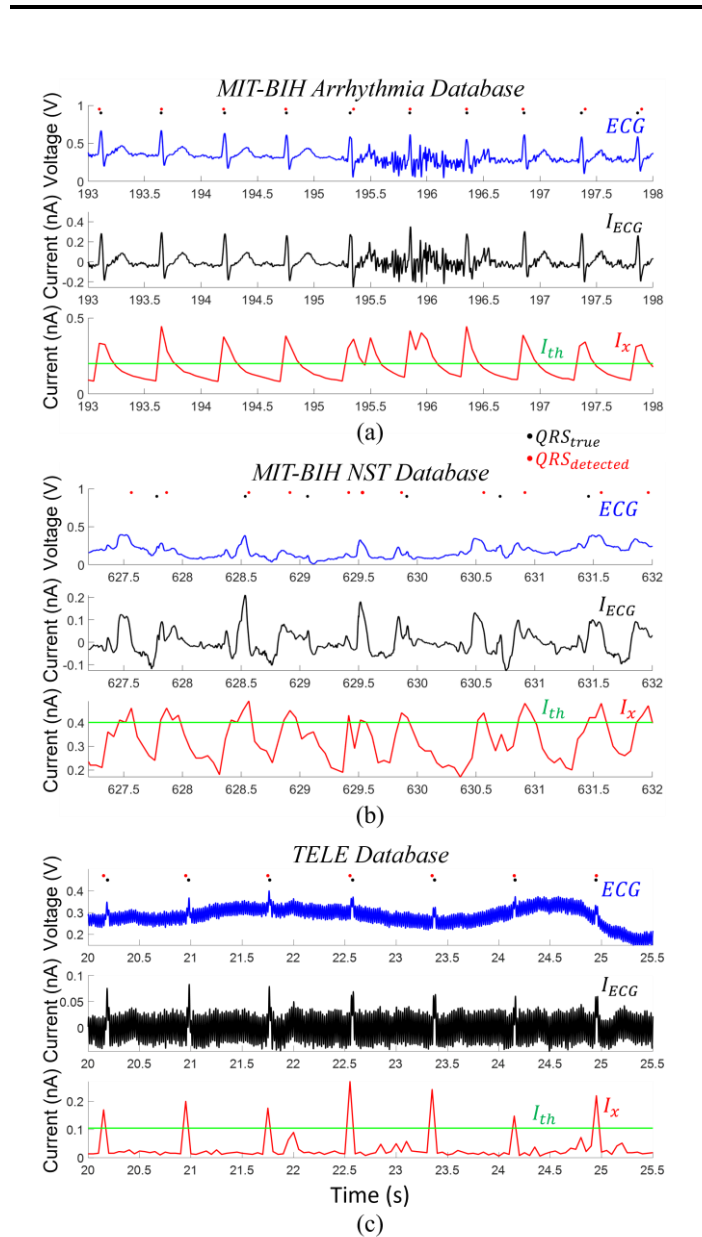


Fig. 14. 5 s portions of sample waveforms for poor quality noisy recordings from the (a) MIT-BIH Arrhythmia (Recording 215,  $\Delta SNR = 6.8~dB$ ), (b) MIT-BIH NST (Recording 118e00,  $\Delta SNR = 6.54~dB$ ), and (c) TELE databases (Recording 79,  $\Delta SNR = 14.71~dB$ ). For each recording; the raw ECG signal; the high-pass filter output,  $I_{ECG}$ ; and the nonlinear filter output  $I_{\chi}$  are shown. The true and detected QRS-wave timestamps are given on the top row with black and red dots, respectively.

with the theoretical expectations. The noise suppression and signal enhancement of the nonlinear filter is theoretically analyzed with statistical methods and specifically using the Fokker-Planck equation, which assesses  $\Delta SNR$  with noise. The  $\Delta SNR$  is inversely and exponentially proportional to noise intensity as [37],  $\Delta SNR$   $\alpha \left(\frac{\epsilon \Delta U}{D}\right)^2 exp\left(-\frac{\Delta U}{D}\right)$  where D is the noise intensity,  $\epsilon$  is the input signal amplitude to the nonlinear filter, and  $\Delta U$  is the potential well change by particle movement. For  $\epsilon = 3.23$  and  $\Delta U = 8$ , the Fokker-Planck leads to the dashed curve in Fig. 13.

TABLE I
PERFORMANCE EVALUATION OF THE PROPOSED PROCESSOR ON THE
MIT-BIH ARRHYTHMIA DATABASE

ECG record #	Total # of beats	Se (%)	+P (%)	DER	Acc (%)
101	1865	99.84	99.95	0.2	99.79
104	2229	99.92	99.92	0.17	99.82
114	1879	100	99.84	0.15	99.84
116	2412	99.3	100	0.7	99.3
201	1963	99.95	100	0.05	99.95
207	1860	99.84	91.71	9.2	91.57
208	2955	99.8	100	0.2	99.8
215	3363	99.59	100	0.4	99.59
217	2208	99.91	100	0.09	99.91
222	2483	99.52	100	0.48	99.52
228	2053	99.52	100	0.48	99.52
Remaining	84248	100	100	0	100
Overall	109518	99.94	99.82	0.25	99.76

## D. QRS-Wave Detection Performance on Major ECG Databases

The proposed ECG processor is evaluated using the MIT-BIH Arrhythmia [36], MIT-BIH Noise Stress Test (NST) [38], and Telehealth (TELE) [16] databases.

The MIT-BIH Arrhythmia database [36] includes 48 30-minute ECG recordings, and it is widely used as a benchmarking database for QRS-wave detection.

The MIT-BIH NST database contains 12 30-minute recordings created by adding calibrated amounts of electrode motion artifact noise on two clean recordings from the MIT-BIH Arrhythmia database [38]. The MIT-BIH NST database is used to assess the QRS-wave detection performance of the proposed processor on the noisy ECG signals.

TELE database includes 250 recordings in different lengths measured in telehealth environment while subjects are holding electrodes on their hands. 250 recordings are selected from measurements conducted with 208 subjects [16]. TELE database is also used to evaluate the QRS-wave detection performance on poor quality recordings.

In Fig. 14, example portions of waveforms of high-noise recordings from all three databases along with respective outputs from the processor are shown.

QRS-wave detection performance is assessed using sensitivity (Se), positive predictivity (+P), and F1 score (F1) metrics described as below:

$$Se = \frac{TP}{TP + FN} * 100, +P = \frac{TP}{TP + FP} * 100,$$

$$F1 = \frac{2 * Se * (+P)}{Se + (+P)},$$
(5)

where TP, FN, and FP are respectively the numbers of true positive, false negative, and false positive detections obtained by following the ANSI/AAML EC57 standard [39], which defines the time window used to identify the true positive (TP) and false negative (FN) values after an ECG recording is processed for QRS-wave detection. For each  $QRS_{true}$ , existence of a  $QRS_{detected}$  is investigated through a search within a  $\pm$  150 ms time window around the  $QRS_{true}$ . If a  $QRS_{detected}$  is found, then the TP is incremented. If a  $QRS_{detected}$  is missing, then the FN is incremented. The

TABLE II
PERFORMANCE COMPARISON WITH ULTRA-LOW POWER QRS DETECTORS VALIDATED USING THE MIT-BIH ARRHYTHMIA DATABASE

	Algorithm / Domain	T / T	Perfor	Performance D.		Area
		Type / Technology	Se (%)	+P (%)	Power	$(mm^2)$
This work	Nonlinear filter / Analog	ASIC / 65nm	99.94	99.82	2.2 nW	0.08
Güngör, 2021 [25]	PT-based / Analog	ASIC / 65nm	99.63	99.47	1.2 nW	0.078
Tekeste, 2019 [15]	A-CLT / Digital	ASIC / 65nm	99.3	99.38	6.5 nW <sup>4</sup>	0.1
He, 2015 [19]	Analog	180nm	N/A	N/A	4.8 nW <sup>1</sup>	$0.76^{2}$
Yin, 2021 [20]	Derivative / Digital	ASIC / 65nm	98.22	99.26	81.9 nW	1.77 2
Bose, 2020 [21]	Adaptive Th / Digital	ASIC / 180nm	N/A	N/A	92 nW	0.24 3
Tang, 2021 [40]	Digital	ASIC / 180nm	99.08	99.76	151 nW	0.248

<sup>&</sup>lt;sup>1</sup> For a direct comparison, only the processor blocks of the system are considered. <sup>2</sup> Total active/digital area. <sup>3</sup> Estimated from the annotated die photo.

TABLE III
QRS DETECTION PERFORMANCE OF THE PROCESSOR (MIT-BIH NST)

ECG record #	Total # of beats	Se (%)	+P (%)	F1 Score (%)
118e24	2278	100	100	100
118e18	2278	99.83	99.83	99.83
118e12	2278	100	99.74	99.87
118e06	2278	100	99.7	99.85
118e00	2278	99.87	99.65	99.76
118e 6	2278	99.26	99.65	99.455
$119e\overline{2}4$	1987	100	99.9	99.95
119e18	1987	100	99.95	99.975
119e12	1987	99.95	99.4	99.674
119e06	1987	99.5	97.2	98.337
119e00	1987	99.95	96.1	97.987
119e 6	1987	88.63	94.89	91.653
Overall	25590	98.92	98.84	98.86

TABLE IV QRS DETECTION PERFORMANCE COMPARISON (MIT-BIH NST)

	QRS detection method	Se (%)	+P (%)	F1 Score
This work	Nonlinear filter	98.92	98.84	98.86
Güngör, 2022 [27]	SR	98.65	99.11	98.87
Benitez, 2000 [42]	Hilbert Transform	93.48	90.6	92.02
Merah, 2015 [43]	Stationary WT	95.3	93.98	94.63
Jia, 2020 [41]	CNN	99.25	96.31	97.76
Elgendi, 2013 [44]	Squaring + MA	95.39	90.25	92.74
Pander, 2022 [45]	FCMC	95.27	94.7	94.98
Rahul, 2021 [46]	Third power + AT	97.58	96.04	96.8

SR: Stochastic Resonance, WT: Wavelet Transform, MA: Moving Average, FCMC: Fuzzy c-median Clustering, EMD: Empirical Mode Decomposition, AT: Adaptive Thresholding.

number of false positives (FP) is calculated as the difference of the number of  $QRS_{detected}$  and TP.

The QRS-wave detection performance for the MIT-BIH Arrhythmia database is presented in Table I. In Table I, recordings with non-zero detection error rate (*DER*) are presented as separate lines, while the performance metrics of all remaining recordings with zero *DER* are presented in the last row. The average sensitivity and positive predictivity values for MIT-BIH Arrhythmia database are 99.94% and 99.82%, respectively. A comparison of the proposed processor with the state-of-the-art low-power QRS-wave detectors is presented in Table II. The processor achieves the best detection performance and fits in the most compact form factor, while dissipating 2.2 nW, making it one of the most power-efficient ECG processors.

The QRS-wave detection performance for the MIT-BIH NST database is presented in Table III. The average Se and +P values are 99.84% and 98.95%, respectively. The proposed

TABLE V QRS DETECTION PERFORMANCE COMPARISON (TELE)

	QRS detection method	Se (%)	+P (%)	F1 Score (%)
This work	Nonlinear filter	98.56	98.67	98.37
Khamis, 2016 [16]	UNSW	98.05	95.75	96.88
Pan, 1985 [26] 1	PT	97.33	85.58	91.07
GR, 2015 [47] <sup>1</sup>	GR	95.18	91.94	93.53
Kasnif, 2017 [17]	STAPLE	96.89	98.33	97.60
Arzeno, 2008 [48] <sup>2</sup>	HT + Derivative	93.9	90.6	92.22
Jia, 2020 [41]	CNN	98.99	95.57	97.24
Ganapathy, 2021 [49]	CNN	97.2	98.16	97.67

<sup>&</sup>lt;sup>1</sup> Implemented in [16]. <sup>2</sup> Implemented in [17]. GR: Gutierrez Rivas algorithm, STAPLE: Simultaneous truth and performance level estimation, HT: Hilbert Transform, CNN: Convolutional Neural Network.

processor outperforms other signal processing methods validated on the MIT-BIH NST database (Table IV).

The proposed processor achieves 98.56% average sensitivity and 98.67% average positive predictivity on 250 recordings in the TELE database (Table V). The processor can detect the QRS-waves with better sensitivity than the other methods, except for a convolutional neural network (CNN) approach in [41].

#### V. DISCUSSION

The Tables II, IV, and V summarize the detection performance of the processor on three different databases. As evident from the tables, the processor achieves better detection performance than most algorithms both in Se and +P with the exception being a CNN algorithm. In the MIT-BIH NST and the TELE databases, [41] achieve better Se than the proposed processor. The better performance of the CNN algorithm in [41], is likely related to its complexity (6 layers each with 30 neurons) and the rich dataset of all recordings in the MIT-BIH Arrhythmia, MIT-BIH NST, and TELE databases used to train the network. Additionally, the results are obtained through 5fold cross-validation. In fact, in another CNN algorithm in [49], which has less complexity (2 layers each with 20 neurons) and is trained using limited datasets, the performance is worse than the proposed processor on the TELE database as evident in the Table V. It should be noted that, in terms of F1, which is a balanced metric between Se and +P, the proposed processor outperforms all algorithms including [41]. Notably, using multiple layers in CNN approaches results in high complexity, which necessitate rich datasets for training [41]. On the other hand, the proposed processor has low complexity, and it processes signals in real-time without need for training. The better QRS-wave detection performance of the proposed

<sup>&</sup>lt;sup>4</sup> Simulated power consumption.

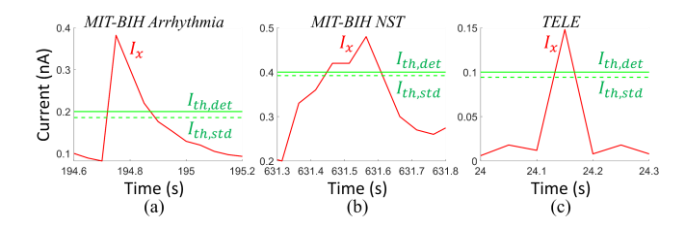


Fig. 15. The empirically-selected threshold values,  $I_{th,det}$ , and the standard deviation of the full recording,  $I_{th,std}$ , almost overlap for three noisy recordings from the three databases. Both values are shown over single QRS-waves of the investigated recordings of (a) #215 of the MIT-BIH Arrhythmia database, (b), #118e00 of the MIT-BIH NST database, and (c) #79 of the TELE database.

processor with low-complexity in real-time marks superiority of the processor over CNN algorithms.

The QRS-wave detection performance results ascribe the significant noise suppression and ORS-wave enhancement performance of the proposed nonlinear filter. Specifically, the optimized a and  $\gamma$  values in (2) are shown to be robust against different recording conditions and subjects. It is noteworthy that, the selection of threshold level is another critical factor leading to the high detection performance. In this work, threshold level is kept constant throughout a recording. However, the constant threshold value is selected empirically as multiples of 0.1 nA (i.e., 0.1 nA, 0.2 nA, 0.3 nA, etc.) such that the F1 score is maximized for each recording. Considering the inaccessibility to the true QRS-wave locations in a practical recording, adjusting the threshold level for a recording can be seen as a disadvantage. However, in the future, the selection of the threshold level can be made based on the statistics of the nonlinear filter output,  $I_x$ . In fact, the initial analysis performed on recordings from the databases shows that, the selected threshold value is very similar to the variance of the complete recording (Fig. 15).

To evaluate the consistency and reliability of the proposed processor, Monte Carlo and process corner simulations are performed in Cadence Spectre using a medium-noise recording (#116) from the MIT-BIH Arrhythmia database. The recording is fed to the nonlinear filter to evaluate the SNR improvement variability and to the complete processor to evaluate the QRSwave detection variability. In both cases, the output is exported into MATLAB for the assessment across Monte Carlo iterations and process corners (tt, ff, ss, sf, fs). For the Monte Carlo simulations, 100 iterations of simulation are performed on the given recording. The mean SNR improvement of the nonlinear filter across the Monte Carlo and process corner simulations are 50.2 dB and 58.3 dB, respectively. Even though the nonlinear filter has relatively high SNR improvement standard deviations across Monte Carlo and process corner simulations  $(\pm 10.96 \, dB \text{ and } \pm 16.44 \, dB, \text{ respectively}), \text{ the QRS-wave}$ detection performance of the proposed processor is distinctly consistent across both Monte Carlo and process corner simulations. Specifically, QRS-wave detection sensitivity is simulated as 99.36  $\pm$  0.03% and 99.37  $\pm$  0.07% across Monte Carlo and process corner simulations while positive predictivity is 100% for both cases.

Notably, the processor demonstrates superior F1 detection performance in real time in ultra-low power and compact manners. As evident in the Table II, the proposed ECG

processor offers better detection performance more compactly than all recent processors. Furthermore, the power dissipation is smaller than all recent processors except [25]. It is noteworthy that, when compared with the processor in [25], the proposed processor performs even better on noisy ECG recordings. When only the recordings of the MIT-BIH Arrhythmia database with nonzero DER in Table I are considered, the proposed processor achieves an average F1 score of 99.48%, compared to 98.9% of the [25].

Notably, because the processor in [25] was not evaluated on the noisy MIT-BIH NST and the TELE databases, it is not possible to make an additional direct detection performance comparison of the two processors. However, comparisons of the numerical implementations of (1) the proposed processor; and (2) the Pan-Tompkins algorithm, the algorithm that the processor in [25] is based on; could potentially serve as an indirect comparison of the approach in this manuscript and the processor in [25]. In fact, such a numerical comparison was made in [27] on the noisy MIT-BIH NST database. The results showed that the nonlinear filter algorithm achieves 98.87% compared to 87.12% of the Pan-Tompkins. It should not be neglected that because of (1) the inherent differences in solving an algorithm numerically in digital and electronically in analog and (2) variations between the analog and digital implementations of the algorithms, this comparison is not direct or conclusive. Nonetheless, as presented in Table IV, the processor proposed in this manuscript and the numerical implementation of the nonlinear filter in [27] yield very similar detection performances as evident by the F1 scores.

It is anticipated that, the QRS-wave detection performance of the proposed processor could be further improved by tuning parameters a and  $\gamma$  on the implemented processor. By enabling tunability of nonlinear filter parameters, the proposed processor is expected to perform better for different types of ECG recordings towards interpatient robustness. In addition, like the digital implementation in [27], the damping coefficient,  $\gamma$ , could be dynamically adjusted based on the ECG amplitude. As such, it could be possible to improve the in-band noise suppression and QRS-wave enhancement performances, which could improve the detection performance.

The remarkable power and area performances can be attributed primarily to facilitation of analog signal processing techniques in implementing the proposed nonlinear filter dynamics. Analog computing, compared to digital, is naturally more appropriate for implementing differential equations as the equation to solve can be simply mapped onto silicon in the form of an analog circuit. Additionally, owing to the several design simplifications presented in Section III, the power and area dissipation are respectively reduced by 42% and 5% compared to the simulation-based study in [28].

There are three major technical contributions of the work. First, the nonlinear filter, which serves as in-band noise suppression and QRS-wave enhancement engine of the processor, is demonstrated as an efficient  $2^{\rm nd}$ -order differential equation solver using current-mode analog signal processing elements of current-mode integrators and current mirrors. The study further discusses how to numerically optimize the key design variables,  $\alpha$  and  $\gamma$ , of the circuit implementation of the filter. Second, the study presents experimental results of functional and performance characterizations of the nonlinear

filter and the other blocks of the processor. For the nonlinear filter, the study demonstrates facilitation of stochastic resonance via the characteristic bell curve shape of SNR improvement with added noise intensity. Additionally, the study presents simulation-based statistical analyses of the full processing chain. Third, the complete processor is validated experimentally using the major ECG database of MIT-BIH Arrhythmia as well as two noisy ECG databases of MIT BIH NST and TELE. The study discusses reasons degrading the detection performance and potential ways to address those in the future.

The significance of this study can be recognized from three different aspects, namely QRS-wave detection performance, efficient ECG processing, and weak signal detection. First, regarding QRS-wave detection, the SNR improvement via inband noise suppression and QRS-wave enhancement reflects onto the QRS-wave detection performance. When evaluated on the major ECG database of the MIT-BIH Arrhythmia, the proposed processor achieves the best QRS-wave detection performance among all ultra-low power ECG processors reported. When evaluated on the noisy ECG databases of the MIT-BIH NST and TELE, the proposed processor achieves one of the best QRS-wave detection performance among the ECG algorithms. Notably, different from the ECG algorithms reporting results for these databases, the proposed processor detects the QRS-waves in real-time as the data streams and in an ultra-low power manner. Second, regarding efficient ECG processing, the proposed processor achieves one of the lowest power and area consumption performance among ultra-low power processors reported. Third, facilitation of stochastic resonance via an ultra-low power real-time nonlinear filter to suppress the in-band noise and enhance the QRS-waves can have uses in other weak signal detection problems in resourcelimited settings such as intracortical neural recording

#### REFERENCES

- [1] M. Shabaan et al., "Survey: smartphone-based assessment of cardiovascular diseases using ECG and PPG analysis," BMC Med Inform Decis Mak, vol. 20, no. 1, p. 177, Jul. 2020, doi: 10.1186/s12911-020-01199-7.
- [2] J. Sztajzel, "Heart rate variability: a noninvasive electrocardiographic method to measure the autonomic nervous system," Swiss Med Wkly, vol. 134, no. 35–36, pp. 514–522, Sep. 2004, doi: 2004/35/smw-10321.
- [3] S. Shah, H. Töreyin, C. B. Güngör, and J. Hasler, "A Real-Time Vital-Sign Monitoring in the Physical Domain on a Mixed-Signal Reconfigurable Platform," *IEEE Transactions on Biomedical Circuits and Systems*, vol. 13, no. 6, pp. 1690–1699, Dec. 2019, doi: 10.1109/TBCAS.2019.2949778.
- [4] K.-R. Lee et al., "A 1.02-μW STT-MRAM-Based DNN ECG Arrhythmia Monitoring SoC With Leakage-Based Delay MAC Unit," *IEEE Solid-State Circuits Letters*, vol. 3, pp. 390–393, 2020, doi: 10.1109/LSSC.2020.3024622.
- [5] Y.-P. Chen et al., "An Injectable 64 nW ECG Mixed-Signal SoC in 65 nm for Arrhythmia Monitoring," *IEEE Journal of Solid-State Circuits*, vol. 50, no. 1, pp. 375–390, Jan. 2015, doi: 10.1109/JSSC.2014.2364036.
- [6] P. Harpe, H. Gao, R. van Dommele, E. Cantatore, and A. H. M. van Roermund, "A 0.20 mm2 3 nW Signal Acquisition IC for Miniature Sensor Nodes in 65 nm CMOS," *IEEE Journal of Solid-State Circuits*, vol. 51, no. 1, pp. 240–248, Jan. 2016, doi: 10.1109/JSSC.2015.2487270.
- [7] Y. H. Jung et al., "Injectable Biomedical Devices for Sensing and Stimulating Internal Body Organs," Advanced Materials, vol. 32, no. 16, p. 1907478, 2020, doi: 10.1002/adma.201907478.

processing in brain-machine interfaces [30], [32], where energy-efficiency and online operation are critical.

It is noteworthy that, the proposed processor is the first ultralow power and real-time ECG processor that is validated on the MIT-BIH NST and TELE databases, which are developed to reflect the different noise sources in practical ECG recording scenarios. The high detection performance of the proposed processor in those recordings potentially suggests robustness in ECG monitoring in mobile subjects. However, integration with an ECG amplifier and investigation of the performance on human subjects during activities of daily life are left as future work.

#### VI. CONCLUSION

This paper presents design and validation of an ultra-low power ECG processor in TSMC 65nm CMOS technology to detect QRS-waves in real time. For energy-efficiency, the processor facilitates analog signal processing techniques implemented using CMOS devices in weak inversion. The high detection performance, which is experimentally validated on a standard ECG database and two noisy ECG databases, is attributed to in-band noise suppression and QRS-wave enhancement performances of a 2<sup>nd</sup> order nonlinear filter. The energy-efficient nonlinear filter is the first ultra-low power implementation that demonstrates stochastic resonance for signal enhancement. With 2.2 nW power dissipation, the processor enables real-time gating signal generation for the power-hungry blocks of an implantable/injectable ECG monitoring system, thereby potentially significantly reducing the overall system power consumption. The design and the results can also potentially pave the way to facilitating stochastic resonance in other online feature extraction applications with tight power budgets.

- [8] J. I. Laughner *et al.*, "A Fully Implantable Pacemaker for the Mouse: From Battery to Wireless Power," *PLOS ONE*, vol. 8, no. 10, p. e76291, Oct. 2013, doi: 10.1371/journal.pone.0076291.
- [9] I. Lee et al., "Circuit techniques for miniaturized biomedical sensors," in Proceedings of the IEEE 2014 Custom Integrated Circuits Conference, Sep. 2014, pp. 1–7. doi: 10.1109/CICC.2014.6946070.
- [10] T. Matić, L. Šneler, and M. Herceg, "An Energy Efficient Multi-User Asynchronous Wireless Transmitter for Biomedical Signal Acquisition," *IEEE Transactions on Biomedical Circuits and Systems*, vol. 13, no. 4, pp. 619–630, Aug. 2019, doi: 10.1109/TBCAS.2019.2917690.
- [11] P. Augustyniak, "Adaptive Sampling of the Electrocardiogram Based on Generalized Perceptual Features," *Sensors*, vol. 20, no. 2, Art. no. 2, Jan. 2020, doi: 10.3390/s20020373.
- [12] L. F. Polanía, R. E. Carrillo, M. Blanco-Velasco, and K. E. Barner, "Exploiting Prior Knowledge in Compressed Sensing Wireless ECG Systems," *IEEE Journal of Biomedical and Health Informatics*, vol. 19, no. 2, pp. 508–519, Mar. 2015, doi: 10.1109/JBHI.2014.2325017.
- [13] C. J. Deepu, X. Zhang, C. H. Heng, and Y. Lian, "A 3-Lead ECG-on-Chip with QRS Detection and Lossless Compression for Wireless Sensors," *IEEE Transactions on Circuits and Systems II: Express Briefs*, vol. 63, no. 12, pp. 1151–1155, Dec. 2016, doi: 10.1109/TCSII.2016.2613564.
- [14] J. Kim et al., "A Wireless Power Transfer Based Implantable ECG Monitoring Device," Energies, vol. 13, no. 4, Art. no. 4, Jan. 2020, doi: 10.3390/en13040905.
- [15] T. Tekeste, H. Saleh, B. Mohammad, and M. Ismail, "Ultra-Low Power QRS Detection and ECG Compression Architecture for IoT Healthcare Devices," *IEEE Transactions on Circuits and Systems I: Regular Papers*, vol. 66, no. 2, pp. 669–679, Feb. 2019, doi: 10.1109/TCSI.2018.2867746.
- [16] H. Khamis, R. Weiss, Y. Xie, C.-W. Chang, N. H. Lovell, and S. J. Redmond, "QRS Detection Algorithm for Telehealth Electrocardiogram Recordings," *IEEE Transactions on Biomedical Engineering*, vol. 63, no. 7, pp. 1377–1388, Jul. 2016, doi: 10.1109/TBME.2016.2549060.

- [17] M. Kashif, S. M. Jonas, and T. M. Deserno, "Deterioration of R-Wave Detection in Pathology and Noise: A Comprehensive Analysis Using Simultaneous Truth and Performance Level Estimation," *IEEE Transactions on Biomedical Engineering*, vol. 64, no. 9, pp. 2163–2175, Sep. 2017, doi: 10.1109/TBME.2016.2633277.
- [18] G. Zheng, G. Fang, R. Shankaran, and M. A. Orgun, "Encryption for Implantable Medical Devices Using Modified One-Time Pads," *IEEE Access*, vol. 3, pp. 825–836, 2015, doi: 10.1109/ACCESS.2015.2445336.
- [19] D. Da He and C. G. Sodini, "A 58 nW ECG ASIC With Motion-Tolerant Heartbeat Timing Extraction for Wearable Cardiovascular Monitoring," *IEEE Transactions on Biomedical Circuits and Systems*, vol. 9, no. 3, pp. 370–376, Jun. 2015, doi: 10.1109/TBCAS.2014.2346761.
- [20] Y. Yin et al., "A 2.63 μW ECG Processor With Adaptive Arrhythmia Detection and Data Compression for Implantable Cardiac Monitoring Device," *IEEE Transactions on Biomedical Circuits and Systems*, vol. 15, no. 4, pp. 777–790, Aug. 2021, doi: 10.1109/TBCAS.2021.3100434.
- [21] S. Bose, B. Shen, and M. L. Johnston, "A Batteryless Motion-Adaptive Heartbeat Detection System-on-Chip Powered by Human Body Heat," *IEEE Journal of Solid-State Circuits*, vol. 55, no. 11, pp. 2902–2913, Nov. 2020, doi: 10.1109/JSSC.2020.3013789.
- [22] X. Liu et al., "A 457 nW Near-Threshold Cognitive Multi-Functional ECG Processor for Long-Term Cardiac Monitoring," *IEEE Journal of Solid-State Circuits*, vol. 49, no. 11, pp. 2422–2434, Nov. 2014, doi: 10.1109/JSSC.2014.2338870.
- [23] L. Yan et al., "A 13 μA Analog Signal Processing IC for Accurate Recognition of Multiple Intra-Cardiac Signals," *IEEE Transactions on Biomedical Circuits and Systems*, vol. 7, no. 6, pp. 785–795, Dec. 2013, doi: 10.1109/TBCAS.2013.2297353.
- [24] N. Bayasi, T. Tekeste, H. Saleh, B. Mohammad, A. Khandoker, and M. Ismail, "Low-Power ECG-Based Processor for Predicting Ventricular Arrhythmia," *IEEE Transactions on Very Large Scale Integration (VLSI) Systems*, vol. 24, no. 5, pp. 1962–1974, May 2016, doi: 10.1109/TVLSI.2015.2475119.
- [25] C. B. Güngör, P. P. Mercier, and H. Töreyin, "A 1.2nW Analog Electrocardiogram Processor Achieving a 99.63% QRS Complex Detection Sensitivity," *IEEE Transactions on Biomedical Circuits and Systems*, vol. 15, no. 3, pp. 617–628, Jun. 2021, doi: 10.1109/TBCAS.2021.3092729.
- [26] J. Pan and W. J. Tompkins, "A Real-Time QRS Detection Algorithm," IEEE Transactions on Biomedical Engineering, vol. BME-32, no. 3, pp. 230–236, Mar. 1985, doi: 10.1109/TBME.1985.325532.
- [27] C. B. Güngör, P. P. Mercier, and H. Töreyin, "A Stochastic Resonance Electrocardiogram Enhancement Algorithm for Robust QRS Detection," *IEEE Journal of Biomedical and Health Informatics*, vol. 26, no. 8, pp. 3743–3754, Aug. 2022, doi: 10.1109/JBHI.2022.3178109.
- [28] C. B. Güngör, P. P. Mercier, and H. Töreyin, "A 3.75 nW Analog Electrocardiogram Processor Facilitating Stochastic Resonance for Real-Time R-wave Detection," in 2021 IEEE Biomedical Circuits and Systems Conference (BioCAS), Oct. 2021, pp. 1–6. doi: 10.1109/BioCAS49922.2021.9645028.
- [29] L. Gammaitoni, P. Hänggi, P. Jung, and F. Marchesoni, "Stochastic resonance," Rev. Mod. Phys., vol. 70, no. 1, pp. 223–287, Jan. 1998, doi: 10.1103/RevModPhys.70.223.
- [30] C. B. Güngör, P. P. Mercier, and H. Töreyin, "Investigating well potential parameters on neural spike enhancement in a stochastic-resonance preemphasis algorithm," *J. Neural Eng.*, vol. 18, no. 4, p. 046062, May 2021, doi: 10.1088/1741-2552/abfd0f.
- [31] F. Guo, Y.-R. Zhou, S.-Q. Jiang, and T.-X. Gu, "Stochastic resonance in a mono-stable system with multiplicative and additive noise," *J. Phys. A: Math. Gen.*, vol. 39, no. 45, p. 13861, Oct. 2006, doi: 10.1088/0305-4470/39/45/002.
- [32] C. B. Güngör and H. Töreyin, "Facilitating stochastic resonance as a preemphasis method for neural spike detection," *J. Neural Eng.*, vol. 17, no. 4, p. 046047, Sep. 2020, doi: 10.1088/1741-2552/abae8a.
- [33] F. Khateb, T. Kulej, M. Akbari, and M. Kumngern, "0.5-V High Linear and Wide Tunable OTA for Biomedical Applications," *IEEE Access*, vol. 9, pp. 103784–103794, 2021, doi: 10.1109/ACCESS.2021.3098183.
- [34] F. Khateb, P. Prommee, and T. Kulej, "MIOTA-Based Filters for Noise and Motion Artifact Reductions in Biosignal Acquisition," *IEEE Access*, vol. 10, pp. 14325–14338, 2022, doi: 10.1109/ACCESS.2022.3147665.
- [35] P. K. Jha, M. K. Rajendran, P. K. Lenka, A. Acharyya, and A. Dutta, "A Fully Analog Autonomous QRS Complex Detection and Low-Complexity Asystole, Extreme Bradycardia, and Tachycardia Classification System," *IEEE Transactions on Instrumentation and Measurement*, vol. 71, pp. 1–13, 2022, doi: 10.1109/TIM.2022.3216392.

[36] G. B. Moody and R. G. Mark, "The impact of the MIT-BIH Arrhythmia Database," *IEEE Eng. Med. Biol. Mag.*, vol. 20, no. 3, pp. 45–50, Jun. 2001, doi: 10.1109/51.932724.

- [37] W. C. Stacey and D. M. Durand, "Stochastic Resonance Improves Signal Detection in Hippocampal CA1 Neurons," *Journal of Neurophysiology*, vol. 83, no. 3, pp. 1394–1402, Mar. 2000, doi: 10.1152/jn.2000.83.3.1394.
- [38] G. B. Moody, W. Muldrow, and R. G. Mark, "The MIT-BIH Noise Stress Test Database." physionet.org, 1992. doi: 10.13026/C2HS3T.
- [39] "ANSI/AAMI EC57:1998/(R)2003 Testing and reporting performance results of cardiac rhythm and ST segment measurement algorithms." https://webstore.ansi.org/standards/aami/ansiaamiec5719982003 (accessed Aug. 15, 2021).
- [40] X. Tang and W. Tang, "An ECG Delineation and Arrhythmia Classification System Using Slope Variation Measurement by Ternary Second-Order Delta Modulators for Wearable ECG Sensors," *IEEE Transactions on Biomedical Circuits and Systems*, vol. 15, no. 5, pp. 1053–1065, Oct. 2021, doi: 10.1109/TBCAS.2021.3113665.
- [41] M. Jia, F. Li, J. Wu, Z. Chen, and Y. Pu, "Robust QRS Detection Using High-Resolution Wavelet Packet Decomposition and Time-Attention Convolutional Neural Network," *IEEE Access*, vol. 8, pp. 16979–16988, 2020, doi: 10.1109/ACCESS.2020.2967775.
- [42] D. S. Benitez, P. A. Gaydecki, A. Zaidi, and A. P. Fitzpatrick, "A new QRS detection algorithm based on the Hilbert transform," in *Computers in Cardiology 2000. Vol.27 (Cat. 00CH37163)*, Sep. 2000, pp. 379–382. doi: 10.1109/CIC.2000.898536.
- [43] M. Merah, T. A. Abdelmalik, and B. H. Larbi, "R-peaks detection based on stationary wavelet transform," *Computer Methods and Programs in Biomedicine*, vol. 121, no. 3, pp. 149–160, Oct. 2015, doi: 10.1016/j.cmpb.2015.06.003.
- [44] M. Elgendi, "Fast QRS Detection with an Optimized Knowledge-Based Method: Evaluation on 11 Standard ECG Databases," *PLOS ONE*, vol. 8, no. 9, p. e73557, Sep. 2013, doi: 10.1371/journal.pone.0073557.
- [45] T. Pander, "A new approach to adaptive threshold based method for QRS detection with fuzzy clustering," *Biocybernetics and Biomedical Engineering*, vol. 42, no. 1, pp. 404–425, Jan. 2022, doi: 10.1016/j.bbe.2022.02.007.
- [46] J. Rahul, M. Sora, and L. D. Sharma, "Dynamic thresholding based efficient QRS complex detection with low computational overhead," *Biomedical Signal Processing and Control*, vol. 67, p. 102519, May 2021, doi: 10.1016/j.bspc.2021.102519.
- [47] R. Gutiérrez-Rivas, J. J. García, W. P. Marnane, and Á. Hernández, "Novel Real-Time Low-Complexity QRS Complex Detector Based on Adaptive Thresholding," *IEEE Sensors Journal*, vol. 15, no. 10, pp. 6036–6043, Oct. 2015, doi: 10.1109/JSEN.2015.2450773.
- [48] N. M. Arzeno, Z.-D. Deng, and C.-S. Poon, "Analysis of First-Derivative Based QRS Detection Algorithms," *IEEE Transactions on Biomedical Engineering*, vol. 55, no. 2, pp. 478–484, Feb. 2008, doi: 10.1109/TBME.2007.912658.
- [49] N. Ganapathy, R. Swaminathan, and T. M. Deserno, "Adaptive learning and cross training improves R-wave detection in ECG," *Computer Methods and Programs in Biomedicine*, vol. 200, p. 105931, Mar. 2021, doi: 10.1016/j.cmpb.2021.105931.